AIAA JOURNAL
Vol. 30, No. 3, March 1992

Numerical Investigation of Vortex Breakdown on a Delta Wing

Shreekant Agrawal,* Raymond Matt Barnett,† and Brian Anthony Robinson‡
McDonnell Douglas Corporation, St. Louis, Missouri 63166

A numerical investigation of leading-edge vortex breakdown on a delta wing at high angles of attack is presented. The analysis has been restricted to low-speed flows on a flat-plate wing with sharp leading edges. Both Euler and Navier-Stokes (assuming fully laminar and turbulent flows) equations have been used in this study and the results are compared against experimental data. Predictions of vortex breakdown progression with angle of attack with both Euler and Navier-Stokes equations are shown to be consistent with the experimental data. However, the Navier-Stokes predictions show significant improvements in breakdown location at angles of attack where the vortex breakdown approaches the wing apex. The location of the primary vortex and the level of vorticity in the prebreakdown regions are affected very little by the viscous effects. In the postbreakdown regions, however, the levels of vorticity in the primary vortex have increased differences between the Euler and Navier-Stokes solutions. Navier-Stokes solutions indicate the presence of a secondary vortex even after the primary vortex is burst. The predicted trajectories of the primary vortex are in very good agreement with the test data with the laminar solutions providing the overall best comparison.

Introduction

THE accurate calculation of vortical flows is a very important yet challenging task in the design of modern fighter aircraft that are required to maneuver at high angles of attack. A flat-plate delta wing with sharp leading edges presents a simple configuration for the study of vortical flows. At sufficiently high angles of incidence the dominant feature of flows over such wings is a pair of counter-rotating vortices (the so-called primary or leading-edge vortices). These vortices form over the upper surface of the wing as a result of the roll-up of the vortex sheet shed from the leading edges. The flow induced by these primary vortices can separate near the wing surface due to the adverse pressure gradient the flow encounters in the spanwise direction.[1] This separated flow may then form an oppositely rotating secondary vortex, which tends to move the primary vortex inboard and away from the wing upper surface. These secondary vortices can also form tertiary vortices by the same process. The formation of these vortices over delta wings has been successfully demonstrated in a number of numerical solutions of the Navier-Stokes equations.[2-7]

The leading-edge vortices at high angles of incidence can experience a phenomenon called breakdown or "burst." The vortex breakdown is characterized by a sudden deceleration of the axial flow in the vortex core, and a decrease in the circumferential velocity associated with the rapid expansion of the vortex core.[8-15] Typically, this process occurs over a distance on the order of the vortex core size and results in the vortex core transitioning from a well-defined vortical structure before burst to a more diffuse structure with milder velocity gradients and higher levels of turbulence after the burst. The location of burst on a delta wing is seen to move forward toward the wing apex with increasing angle of attack. The bursting of the vortex on an aircraft may result in several adverse effects, e.g., abrupt change in pitching moment, loss in lift, buffet, and so on, and can be a strict limitation of its maneuverability. Effects of the bursting may be felt not only by the individual aerodynamic surfaces on which the bursting occurs, but also on those in their close proximity. Realistic flow calculation about an aircraft at high angles of attack, therefore, requires an accurate prediction of vortex breakdown. While the leading-edge vortex and vortex breakdown have been studied extensively by researchers, there is currently no universally accepted theory on the mechanism of breakdown. Analytical efforts have been restricted to only simplified vortex models without including the presence of the wing.[16,17]

Numerical solutions obtained using Euler equations have recently been shown to be qualitatively, and somewhat quantitatively, realistic for sharp-edged delta wings.[8-10,18] There has also been speculation that the leading-edge vortex breakdown is governed primarily by inviscid effects and that the viscous effects are only secondary.[9,10] However, one would expect that the viscous effects would strongly affect the inviscid results if the pressure gradients in the vortex core due to the burst are large. Also, the effects of secondary and tertiary vortices, as observed in the Navier-Stokes solutions, are absent in the Euler results. Such details of the vortical flowfield can only be obtained from the Navier-Stokes equations.

The intent of the present study is to analyze in detail the differences between Euler and Navier-Stokes solutions on a delta wing at high angles of attack, with a particular emphasis on predicting flowfields before and after the occurrence of vortex breakdown. Differences between the inviscid and viscous solutions are addressed in order to determine which set of equations best predicts the flow in the pre- and postbreakdown regions. The geometry chosen for this study is a flat-plate semispan delta wing with a leading-edge sweep of 70 deg and a 25-deg bevel on the lower surface along the leading and trailing edges as shown in Fig. 1. An extensive experimental database exists for this configuration.[19,20] The database consists of flow visualization, force and moment, surface pressures, three-component laser Doppler velocimetry (LDV), and seven-hole probe flowfield surveys. The results for this analysis were computed using an Euler/Navier-Stokes code, CFL3D,[2] briefly described in the next section.

Numerical Method

The computational algorithm in CFL3D is based on a thin-layer approximation of the three-dimensional, time-dependent, conservation law form of the compressible Navier-Stokes equations. The code solves the discretized flow equations im-

Received Oct. 18, 1990; revision received June 21, 1991; accepted for publication July 18, 1991.

*Technical Specialist–Aerodynamics, CFD Project, McDonnell Aircraft Company. Associate Fellow AIAA.

†Senior Engineer–Aerodynamics, Aerodynamic Technology, McDonnell Aircraft Company. Member AIAA.

‡Engineer–Aerodynamics, CFD Project, McDonnell Aircraft Company. Member AIAA.

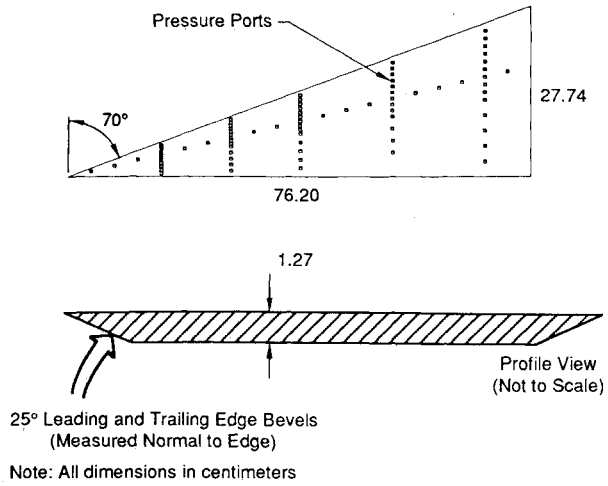

Fig. 1 Flat-plate semispan delta wing model.

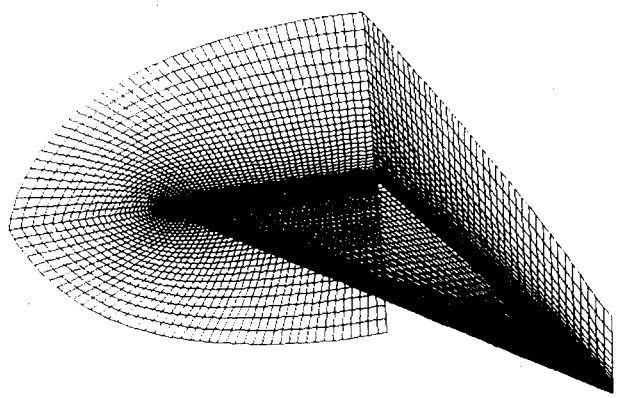

Fig. 2 Partial view of the computational mesh for delta wing. Medium mesh: 61 (axial) × 65 (radial) × 89 (circumferential).

plicitly using an upwind-biased spatial differencing scheme with either flux difference splitting or flux vector splitting for the convective and pressure terms, and central differencing for the shear stress and heat transfer terms. In this study the Roe-averaged flux difference splitting scheme was applied for the spatial differencing. This scheme does not require the addition of artificial dissipation terms which can adversely affect the solution. Flux limiting is also used to alleviate oscillations near high-gradient regions such as shock waves. The Baldwin-Lomax turbulence model is used to calculate the turbulent viscosity. This code is used extensively in the aerospace industry and has been verified for numerous geometries and flow conditions.

Mesh Topology

An H-O-type mesh topology for a half-plane model of the delta wing was used in this study. The half-plane wing was used to provide the best mesh resolution around the wing for a given number of points. The mesh was constructed by successive generation of two-dimensional O-type meshes normal to the wing centerline. These were generated using a computer program that solves an elliptic system of partial differential equations.[21] It automatically sections the cross-plane domain into a number of simpler domains based on singular points on the surface geometry, such as the wing leading edge. High-quality meshes are first generated on these simpler domains and then matched smoothly at their common boundaries. This procedure results in a highly orthogonal mesh near difficult areas, such as the sharp leading edges of the wing. The surface mesh along with the symmetry plane and a crossflow plane is shown in Fig. 2. The mesh dimensions are 61 (axial), 65 (radial), and 89 (circumferential). These dimensions were used for most of the analyses, and will be referred to as the medium mesh. A mesh-embedding technique was also utilized to refine the medium mesh around the leading edge and the upper surface of the wing from the apex to the trailing edge. The extent of embedding in the normal direction was just far enough to include the region where most of the vortical flow phenomenon is observed. Such a refinement of the medium mesh yielded an embedded region with dimensions 81 (axial), 87 (radial), and 133 (circumferential). In addition, a few calculations were performed on a mesh of dimensions 61 × 33 × 89, to be referred to as the coarse mesh in this paper.

Results

Calculations were performed at a freestream Mach number, $M_\infty = 0.3$ and several angles of attack (α). The Reynolds number based on the root chord (Re_c) was one million. While only steady-state solutions were sought, there were indications of unsteadiness in the flow solutions at the higher angles of attack. The level of unsteadiness, however, appeared to be quite small as the fluctuations in lift, drag, and pitching moment coefficients at the assumed steady-state conditions were less than 1% for most calculations. Solution convergence on the medium mesh was achieved in approximately 3 CPU hours on a Cray-2 computer. On the coarse mesh, runs were executed on a Cray-XMP, and convergence was reached in a CPU time equivalent to 1 hour of CPU on the Cray-2. The average residuals were reduced by approximately 2–3 orders of magnitude in 1000–2000 iterations, depending on the mesh size and angle of attack. At the higher angles of attack, where vortex breakdown is observed over the wing, the solution convergence was slower, although it was always possible to achieve convergence of integrated forces and moments. Navier-Stokes solutions were obtained using either a fully laminar or a fully turbulent flow model. Results from these calculations are shown in Fig. 3–14.

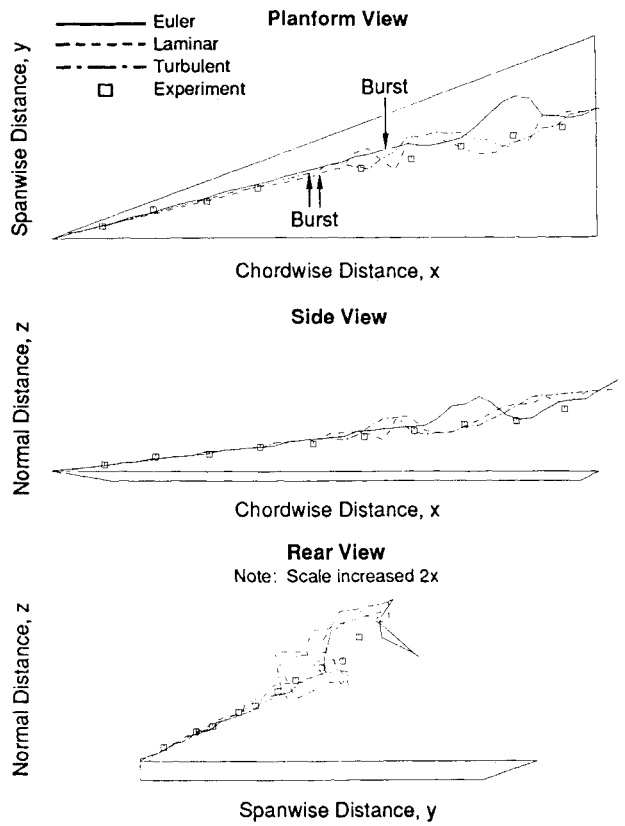

Fig. 3 Comparison of predicted vortex location with test data. Medium mesh, $M_\infty = 0.30$, $Re_c = 1 \times 10^6$, $\alpha = 30$ deg.

The locations or trajectories of the leading-edge vortex from the Euler and Navier-Stokes solutions for $\alpha = 30$ deg, using the medium mesh, are shown in Fig. 3. Three orthogonal views of the wing are given in this figure to define completely the primary vortex location relative to the wing. Available flow visualization data are also shown. The vortex location from the computed solutions was identified by locating the points of minimum total pressure in the primary vortex at each axial station. The computational solutions, in general, show excellent agreement with each other and the experimental data before vortex breakdown occurs (as indicated on the plots). A closer inspection of the planform views in Fig. 3 indicates that the vortex location from the Euler solutions is slightly outboard of the other data. The leading-edge vortices in the laminar and turbulent solutions are further inboard, which gives somewhat better agreement with the experimental data. Such a trend in these solutions is not too surprising, as the secondary vortex usually outboard of the primary one is absent in the Euler solutions. This secondary vortex displaces the primary vortex inboard and slightly upward. Another point worth noting here is that the laminar solution overall provides the best comparison with the test data.

Figure 3 also shows that the vortex follows an almost linear path in the prebreakdown region, whereas the path becomes random beyond the breakdown. After vortex breakdown has occurred, the point of minimum total pressure, which was used to define the vortex center, can be seen to enter a swirling-type motion as it moves downstream. This swirling of the vortex center is consistent with the behavior observed experimentally in what is referred to as a spiral-type vortex breakdown.[11] The experimental data shown is from flow visualization of the leading-edge vortex using smoke and a thin laser light sheet. A video image of the flow visualization was digitized and the approximate location of the vortex center selected by visual inspection.[20] Since the video images of the vortex after breakdown show only a large diffuse vortex core area, the center was selected, and therefore no spiraling motion is observed in the experimental data.

The vortex sheet or shear layer shed from the leading edge of the delta wing rolls up above the wing to form the primary vortex. It is possible to trace the location of this sheet by plotting the locus of maximum swirl in an axial plane.[10] These plots are created by performing radial surveys outward from the vortex center. The point of maximum swirl along these lines is determined by linear interpolation of the available data. By plotting the maximum swirl points along the different radial lines, the sheet position can be determined. Shown in Fig. 4 is a comparison of the shear layers determined by this method for the CFL3D solutions and the laser Doppler experimental data. The trend in vortex locations shown in this figure is similar to that shown in Fig. 3 for vortex centers. Again, the Euler solution shows the most outboard location of the primary vortex and the laminar solution the most inboard. Some jaggedness is apparent in the shape of these curves due to the linear interpolation and a relatively coarse mesh size.

The lift coefficients obtained from the CFL3D solutions are shown in Fig. 5. The predicted values of lift are in fair agreement with the experimental data except for $\alpha \geq 30$ deg. However, the experimental values can be seen to be offset from the computational results. The negative camber produced by the lower surface bevel on the leading and trailing edges of the delta wing produces a shift in the point of zero lift predicted by the computational codes. The experimental data show less effects from this negative camber due to flow separation on the trailing-edge bevel. The predictions of pitching moment (not shown here) suffer from the same problem as the lift. It appears that the separation on the beveled surfaces is not being modeled with the medium mesh used for most of the analysis.

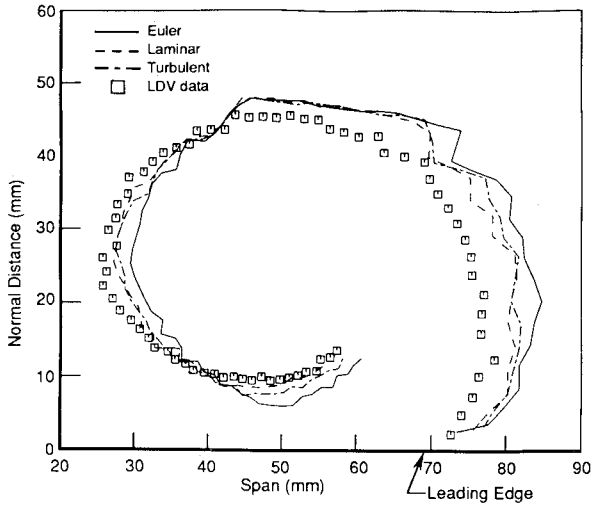

Fig. 4 Comparison of shear layers defined by the locus of maximum swirl. Medium mesh, $M_\infty = 0.30$, $\alpha = 30$ deg, $Re_c = 1 \times 10^6$, $x/c = 0.25$.

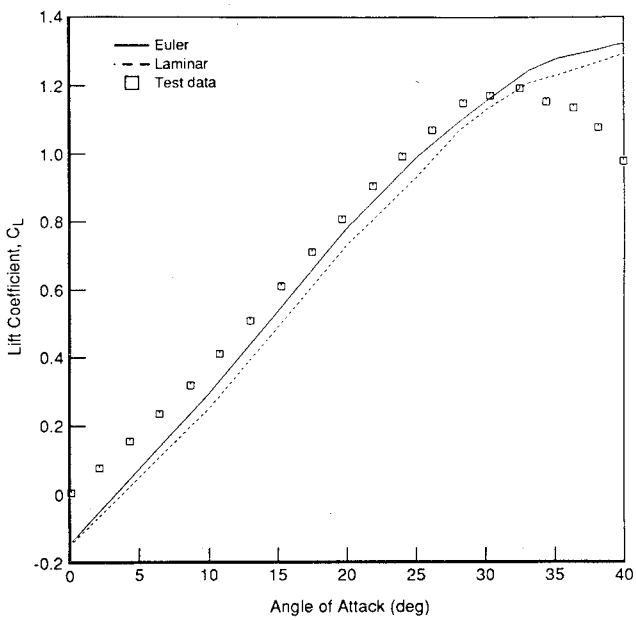

Fig. 5 Comparison of predicted lift with test data. Medium mesh, $M_\infty = 0.30$, $\alpha = 30$ deg, $Re_c = 1 \times 10^6$.

The peak suction pressures on the upper surface of the wing at each axial station are shown in Fig. 6. The experimental data from the row of pressure taps along the 65% local span stations, which also corresponded to the peak suction pressures, are shown for comparison with these data. The Euler solutions are seen to predict higher peak suction pressures on the wing than the Navier-Stokes solutions. The breakdown locations, which correspond to those marked in Fig. 3, are also indicated.

Figure 7 shows the particle traces from the Euler, laminar, and turbulent solutions on the medium mesh, at $\alpha = 30$ deg. This gives a qualitative picture of the flowfields in the leading-edge vortex. The abrupt change in the traces from a regular, ordered structure is an indication of the vortex breakdown occurring in the flowfield, which is clearly illustrated in this figure. Also, it appears that at a fixed angle of attack the breakdown moves aft if the viscous effects are not included. The breakdown location was identified by inspection of the streamwise component of velocity on each axial mesh plane

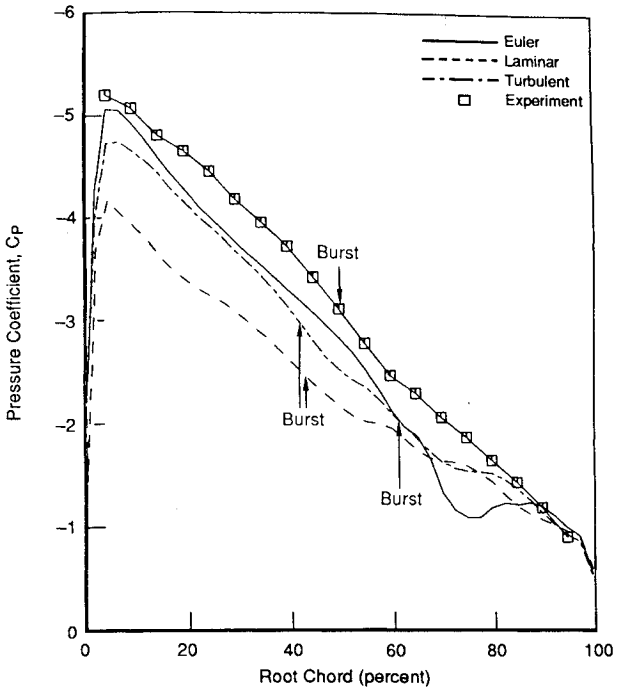

Fig. 6 Maximum negative surface pressure coefficients. Medium mesh, $M_\infty = 0.30$, $\alpha = 30$ deg, $Re_c = 1 \times 10^6$.

using a postprocessor, PLOT3D.[22] A rapid decrease in this velocity component and increase in vortex core size are observed at the onset of vortex breakdown.

At this point, a more refined criterion to determine the burst location is in order. While PLOT3D gives a reasonably good idea of the breakdown regions, the precise location of the onset of vortex breakdown from the computational results was determined by inspecting the axial velocity distribution in the leading-edge vortex. To accomplish this, the location of the vortex core was determined using the point of minimum total pressure, which was then used to determine an average angular orientation, before burst, of the vortex relative to the wing centerline and the upper surface of the wing. The vortex trajectory was then approximated as being a straight line originating at the apex of the wing and the velocities were transformed to this new coordinate system. The transformed axial velocities were inspected using contour plots as shown in Fig. 8. Before breakdown, the axial velocity is shown to increase to a single peak value at the vortex center. With the onset of vortex breakdown, the axial velocity at the core of the vortex begins stagnating and shows significant asymmetry. The burst point was thus determined by locating the axial station where the axial velocities were first observed to have a depressed region (i.e., no longer a single peak value).

The progression of the vortex breakdown location with increasing angle of attack was determined from the Euler, laminar, and turbulent solutions for the medium mesh. The sensitivity of the flowfields to mesh refinement is evaluated by

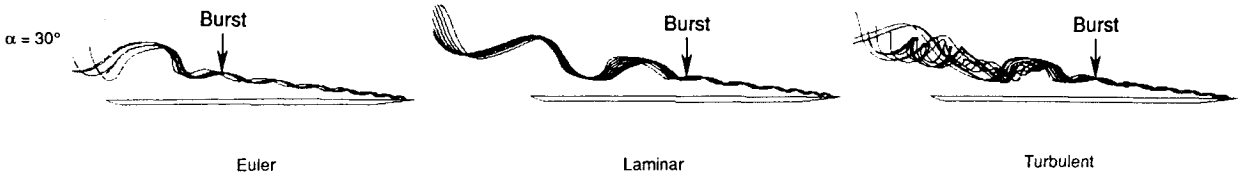

Fig. 7 Vortex breakdown regions indicated with particle traces. Medium mesh, $M_\infty = 0.30$, $Re_c = 1 \times 10^6$.

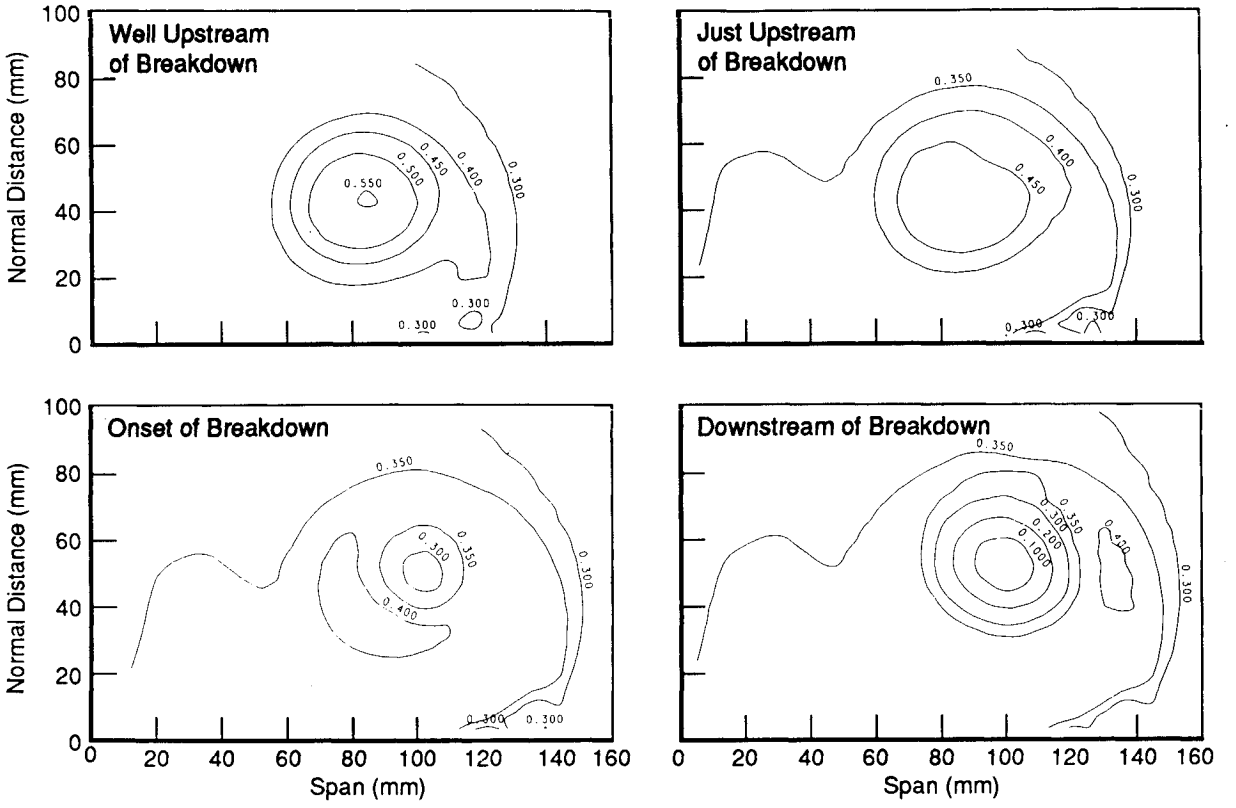

Fig. 8 Identifying vortex breakdown from axial velocity contours. Medium mesh, $M_\infty = 0.30$, $\alpha = 30$ deg, $Re_c = 1 \times 10^6$.

comparison of coarse mesh breakdown locations (Fig. 9) with those of the medium mesh (Fig. 10). These figures show the quantitative predictions of the breakdown locations for various angles of attack along with the experimental data. The breakdown locations shown in Fig. 10 also correlate with those shown in Fig. 7.

It should be noted that both the location and the rate at which the vortex breakdown progresses with the angle of attack are different for the Euler and Navier-Stokes solutions (Figs. 9 and 10). These figures also show that the breakdown location predicted from the laminar solutions better matches experiment than the Euler solutions. This is particularly evident when the angles of attack are above 30 deg, which corresponds to the maximum lift from experiment. Results from the turbulent solutions are found to be similar to the laminar results.

Figures 11 and 12 show the streamwise vorticity contours in the pre- and postbreakdown regions, as determined from the Euler and Navier-Stokes solutions at $\alpha = 30$ deg on the medium mesh. The experimental data and the embedded mesh solution for the laminar case are also included. The experimental data shown in these figures are from LDV surveys with the survey point spacing near the vortex center being about 0.8 mm for $x/c = 0.25$, and 2.2 mm for $x/c = 0.70$. The experimental data were interpolated, where necessary, for use in PLOT3D. The velocities were nondimensionalized by the freestream velocity whereas the physical dimensions were in dimensional units.

A comparison of vorticity levels shows that the computed results have lower maximum values of vorticity in the primary vortex and a slight spreading of the vortical flow relative to the experimental data (Fig. 11). The predicted contour levels in the primary vortex core are very similar, although the maximum value of vorticity in the vortex core is nearly five times greater in the LDV data. Navier-Stokes solutions and the experimental data indicate the presence of a secondary vortex, shown by the negative magnitudes of the vorticity. The laminar solution shows a much larger secondary vortex than the turbulent solution, which is consistent with the observations from previous experiments. Presence of a tertiary vortex having positive vorticity is also seen in the laminar solution with mesh embedding. The Euler solution, as expected, shows no indication of a secondary vortex. The increased resolution with mesh embedding results in more pronounced vortices, as also shown by several researchers.[23,24] The vorticity level in the primary vortex core is significantly higher with the embedded mesh. This gives a closer match with the experimental data as seen from the figure. The level of vorticity in the secondary vortex, on the other hand, is predicted quite well by all the Navier-Stokes solutions. Only laminar calculations were performed with the embedded mesh.

Figure 12 shows the vorticity contours at a location where the primary vortex is burst. The vorticity levels are much smaller than in the prebreakdown region. Another observation is that the secondary vortex is present in the Navier-Stokes solutions even after the primary vortex is burst, but the level of vorticity in the secondary vortex core is lower than that found in the prebreakdown region. The decrease in vorticity level after breakdown is consistent with the experimental data. Figure 12 also shows that the predicted vorticity distribution in the primary vortex after burst is asymmetric. This asymmetric pattern is not exhibited in the LDV data. One possible explanation for this discrepancy is the inability of the CFD method to model properly the increase in the level of turbulence in the burst vortex region, exhibited in the LDV data. In spite of the complex flowfield in the burst vortex region, the overall agreement with experiment is considered to be fair.

The velocity data obtained with the LDV surveys can provide further insight into the reasons for the apparent differences between the computed solutions and the wind tunnel data. A survey of the velocity data along a line parallel to the upper surface of the wing was used to compare the predicted solutions with the LDV data. This line was selected to coincide with the maximum chordwise velocity in the LDV data which should be near the center of the primary vortex. The computed solutions were interpolated on this line and are compared with the test data in Fig. 13. It is readily seen that the computed results do not match either the peak value or the shape of the velocity distribution obtained from the experiment. The medium mesh size apparently does not have sufficient resolution to capture this detail. However, the mesh embedding does improve the predictions at and outboard of the vortex center locations. From this plot, it can be anticipated that further refinement of the mesh near the vortex core is needed to better resolve the high gradients occurring in the primary vortex.

To understand further the breakdown phenomenon, it is helpful to examine the pressure distribution in the vortex core. Figure 14 shows such a plot of pressure coefficients vs the distance from the wing apex for the computed solutions at $\alpha = 30$ deg. The pressures shown are at the same location as the minimum total pressure in the primary vortex. It is readily observed that the suction (negative pressure coefficient) at the center of the vortex increases rapidly as the leading-edge vortex develops above the delta wing. After reaching a peak value near the wing apex, this suction begins to decrease fairly rapidly. The slopes of the three solutions in this area are very close to each other. The breakdown occurs as the adverse pressure gradient becomes large. The locations of vortex burst determined through the inspection of the axial velocity con-

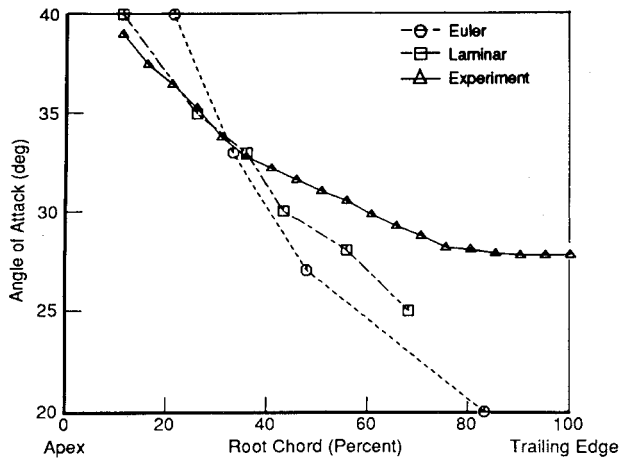

Fig. 9 Vortex breakdown progression with angle of attack. Coarse mesh, $M_\infty = 0.30$, $Re_c = 1 \times 10^6$.

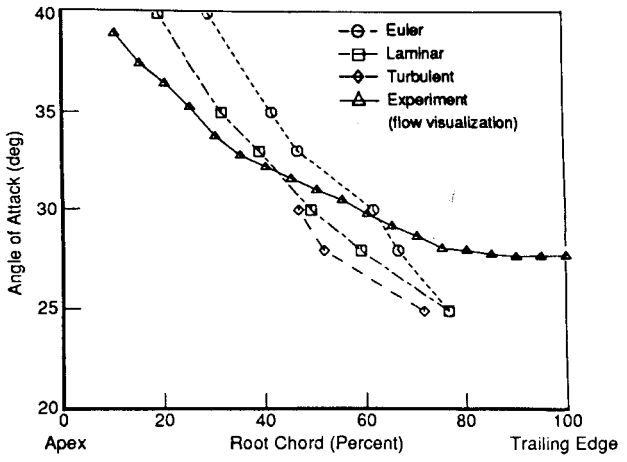

Fig. 10 Vortex breakdown progression with angle of attack. Medium mesh, $M_\infty = 0.30$, $Re_c = 1 \times 10^6$.

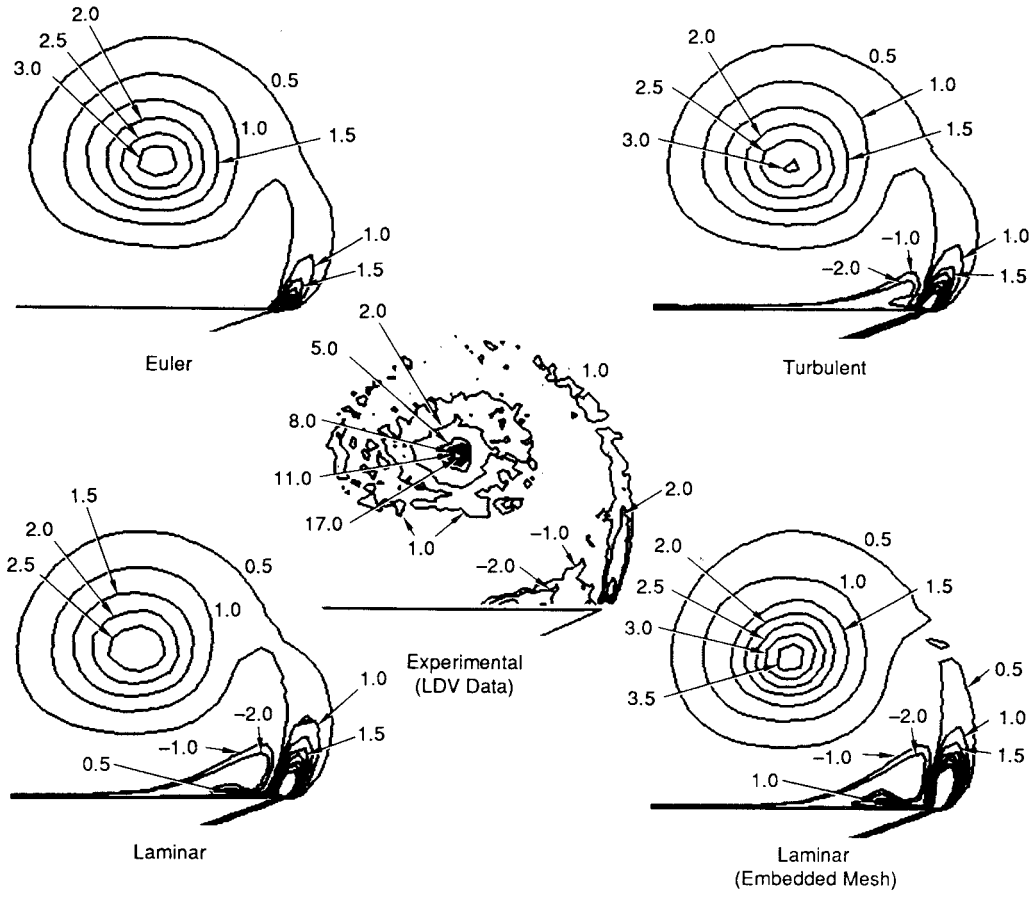

Fig. 11 Comparison of predicted vorticity levels (x-direction) from Euler and Navier-Stokes solutions. Before burst, $M_\infty = 0.30$, $\alpha = 30$ deg, $Re_c = 1 \times 10^6$, $x/c = 0.25$.

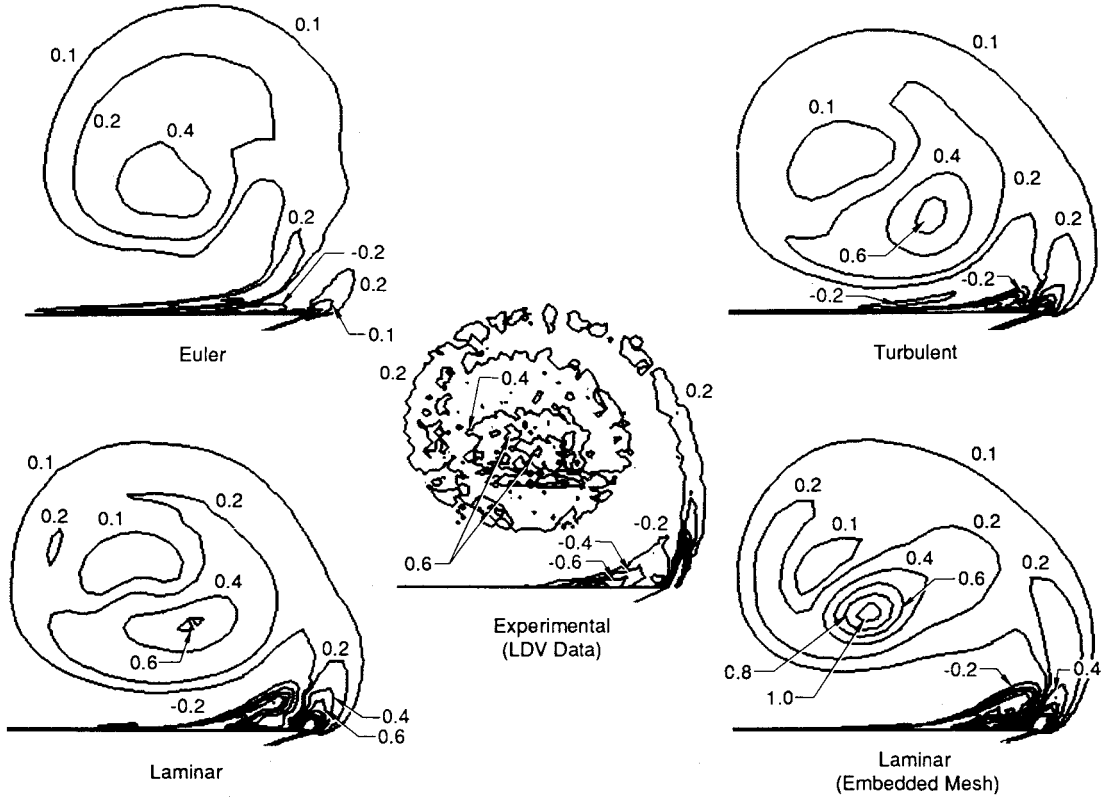

Fig. 12 Comparison of predicted vorticity levels (x-direction) from Euler and Navier-Stokes solutions. After burst, $M_\infty = 0.30$, $\alpha = 30$ deg, $Re_c = 1 \times 10^6$, $x/c = 0.70$.

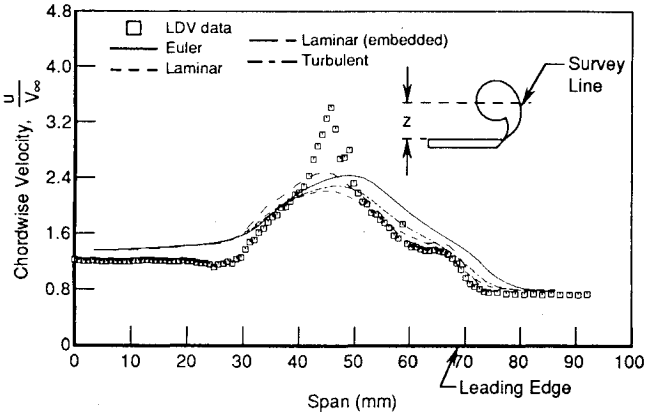

Fig. 13 Comparison of chordwise velocity along a line parallel to the wing. $M_\infty = 0.30$, $Re_c = 1 \times 10^6$, $\alpha = 30$ deg, $x/c = 0.25$, $z = 24.91$ mm.

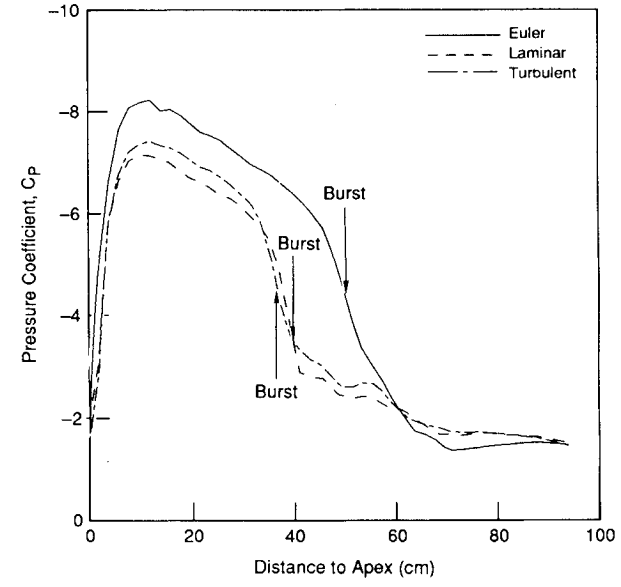

Fig. 14 Pressure coefficients along the vortex core. Medium mesh, $M_\infty = 0.30$, $Re_c = 1 \times 10^6$.

tours are also shown on this figure. Vortex burst is shown to fall approximately in the center of the region where the pressure is increasing most rapidly. This is consistent with the changes in axial velocity in the vortex core in this region.The Euler and Navier-Stokes solutions in the figure show fairly similar trends in pressure in the vortex core. The Euler solution, however, shows a stronger vortex before breakdown, which is consistent with the other comparisons made in previous figures.

Other issues not addressed in this study may prove to be important in more accurate prediction of vortex breakdown. For example, the meshes used here are not usually considered fine enough for resolving flowfields in the primary vortex region. Mesh embedding may offer improved predictions of vortex breakdown.[25,26] The standard Baldwin-Lomax turbulence model may not be adequate for vortical flows at high angles of attack.[27] Transition model may also play a role in such calculations. Finally, the wind tunnel walls may affect the vortex breakdown location.

Conclusions

A numerical investigation of leading-edge vortex breakdown at high angles of attack was conducted on a flat-plate delta wing with sharp leading and trailing edges. Predicted solutions of Euler, laminar, and turbulent Navier-Stokes equations were compared against an extensive experimental database. The vortex breakdown progression with angle of attack with both Euler and Navier-Stokes equations was found to be consistent with the experimental data. The Navier-Stokes solutions, however, showed significant improvements in breakdown location at angles of attack where the vortex breakdown approached the wing apex.

The locations of the primary vortex predicted by the solutions were in very good agreement with the test data, particularly in the prebreakdown region. The laminar solutions provided the overall best comparison. Relative to experiment, the Euler solutions showed a small displacement of the primary vortex due to the lack of secondary vortex in these solutions.

The location of the primary vortex and the level of vorticity in the prebreakdown regions in these flowfield solutions were affected very little by the viscous effects, even though the Navier-Stokes solutions exhibited viscous phenomena such as secondary and tertiary vortices. The tertiary vortex was only observed in the laminar solution on an embedded mesh. In the postbreakdown regions, however, the levels of vorticity in the primary vortex had increased differences between the Euler and Navier-Stokes solutions. The predicted vorticity distribution in the primary vortex after burst was found to be asymmetric. Also, the Navier-Stokes solutions indicated the presence of a secondary vortex even after the primary vortex was burst, but the level of vorticity in the secondary vortex core after burst was lower than that found in the prebreakdown region.

Analysis of the pressure distribution in the vortex core indicated that the breakdown occurs as the adverse pressure gradient in the core becomes very large. The Euler and Navier-Stokes solutions showed similar trends in pressure near the vortex core.

Acknowledgments

The original version of this material was first published by the Advisory Group for Aerospace Research and Development, North Atlantic Treaty Organization (AGARD/NATO) in Conference Proceedings CP 494–Vortex Flow Aerodynamics. This study was supported by the McDonnell Douglas Independent Research and Development program. Computer resources for this work were provided by the National Aerodynamic Simulation Facility at the NASA Ames Research Center. The authors would also like to express their sincere thanks to James L. Thomas and Sherrie Krist of the NASA Langley Research Center for providing assistance in executing the latest version of the CFL3D code used in this study. Experimental data were obtained by McDonnell Aircraft Company (MCAIR) in conjunction with McDonnell Douglas Research Laboratories (MDRL) as part of a United States Navy funded investigation of leading-edge vortex behavior on delta wings.

References

[1]Hummel, D., "On the Vortex Formation Over a Slender Wing at Large Angles of Incidence," *AGARD-FDP Symposium on High Angle of Attack Aerodynamics*, AGARD-CPP-247, Oct. 1978, pp. 15.1–15.17.

[2]Thomas, J. L., Taylor, S. L., and Anderson, W. K., "Navier-Stokes Computations of Vortical Flows Over Low Aspect Ratio Wings," AIAA Paper 87-0207, Jan. 1987.

[3]McMillin, S. N., Thomas, J. L., and Murman, E. M., "Euler and Navier-Stokes Solutions for the Leeside Flow Over Delta Wings at Supersonic Speeds," AIAA Paper 87-2270, Aug. 1987.

[4]Rizzi, A., Muller, B., and Purcell, C. J., "Comparison of Euler and Navier-Stokes Solutions for Vortex Flow Over a Delta Wing," AIAA Paper 87-2347, Aug. 1987.

[5]Fujii, K., and Schiff, L. B., "Numerical Simulation of Vortical

Flows over a Strake-Delta Wing," *AIAA Journal*, Vol. 27, Sept. 1989, pp. 1153–1162.

[6]Ekaterinaris, J. A., and Schiff, L. B., "Vortical Flows over Delta Wings and Numerical Prediction of Vortex Breakdown," AIAA Paper 90-0102, Jan. 1990.

[7]Vadyak, J., and Schuster, D. M., "Navier-Stokes Simulation of Burst Vortex Flowfields for Fighter Aircraft at High Incidence," *Journal of Aircraft*, Vol. 28, No. 10, 1991, pp. 638–645.

[8]Hitzel, S. M., and Schmidt, W., "Slender Wings with Leading-Edge Vortex Separation: A Challenge for Panel Methods and Euler Solvers," *Journal of Aircraft*, Vol. 21, No. 10, 1984, pp. 751–759.

[9]Hitzel, S. M., "Wing Vortex Flows Up Into Vortex-Breakdown, A Numerical Simulation," AIAA Paper 88-2518-CP, June 1988, pp. 73–83.

[10]O'Neil, P. J., Barnett, R. M., and Louie, C. M., "Numerical Solution of Leading-Edge Vortex Breakdown Using an Euler Code," AIAA Paper 89-2189, July 1989.

[11]Lambourne, N. C., and Bryer, D. W., "The Bursting of Leading-Edge Vortices—Some Observations and Discussion of the Phenomenon," ARC RM 3282, April 1961.

[12]McKernan, J. F., and Nelson, R. C., "An Investigation of the Breakdown of the Leading-Edge Vortices on a Delta Wing at High Angles of Attack," AIAA Paper 83-2114, Aug. 1983.

[13]Hartwich, P. M., Hsu, C. H., Luckring, J. M., and Liu, C. H., "Numerical Study of the Vortex Burst Phenomenon for Delta Wings," AIAA Paper 88-0505, Jan. 1988.

[14]Leibovich, S., "The Structure of Vortex Breakdown," *Annual Review of Fluid Mechanics*, Vol. 10, 1978, pp. 221–246.

[15]Escudier, M., "Vortex Breakdown: Observations and Explanations," *Progress in Aerospace Sciences*, Vol. 25, 1988, pp. 189–229.

[16]Berger, M. S., "Remarks on Vortex Breakdown," *Proceedings of the Workshop on Mathematical Aspects of Vortex Dynamics*, edited by R. E. Caflisch, April 1988, pp. 171–182.

[17]Hoeijmakers, H. W. M., "Numerical Simulation of Vortical Flows," NLR-MP-86032-U, *Introduction to Vortex Dynamics*, Von Karman Institute for Fluid Dynamics, Rhode-Sait-Génése, Belgium, May 1986.

[18]Raj, P., Sikora, J. S., and Keen, J. M., "Free-Vortex Flow Simulation Using a Three-Dimensional Euler Aerodynamic Method," *Journal of Aircraft*, Vol. 25, No. 2, 1988, pp. 128–134.

[19]O'Neil, P. J., Roos, F. W., Kegelman, J. T., Barnett, R. M., and Hawk, J. D., "Investigation of Flow Characteristics of a Developed Vortex," Final Report, NADC-89114-60, May 1989.

[20]Kegelman, J. T., and Roos, F. W., "Effects of Leading-Edge Shape and Vortex Burst on the Flowfield of a 70-degree-Sweep Delta Wing," AIAA Paper 89-0086, Jan. 1989.

[21]Thompson, J. F., Thames, F. C., and Mastin, C. W., "Automatic Numerical Generation of Body-Fitted Curvilinear Coordinate System for Field Containing Any Number of Arbitrary Two-Dimensional Bodies," *Journal of Computational Physics*, Vol. 15, No. 3, 1974, pp. 299–319.

[22]Buning, G. P., and Steger, J. L., "Graphics and Flow Visualization in Computational Fluid Dynamics," AIAA Paper 85-1507, July 1985.

[23]Fujii, K., "A Method to Increase the Accuracy of Vortical Flow Simulations," AIAA Paper 88-2562-CP, June 1988, pp. 321–328.

[24]Ekaterinaris, J. A., and Schiff,L. B., "Numerical Simulation of the Effects of Variation of Angle of Attack and Sweep Angle on Vortex Breakdown over Delta Wings," AIAA Paper 90-3000-CP, Aug. 1990, pp. 59–67.

[25]Krist, S. L., Thomas, J. L., Sellers, W. L., and Kjelgaard, S. O., "An Embedded Grid Formulation Applied to a Delta Wing," AIAA Paper 90-0429, Jan. 1990.

[26]Powell, K. G., Beer, M. A., and Law, G. W., "An Adaptive Embedded Mesh Procedure for Leading-Edge Vortex Flows," AIAA Paper 89-0080, Jan. 1989.

[27]Degani, D., Schiff, L. B., and Levy, Y., "Physical Considerations Governing Computation of Turbulent Flows Over Bodies at Large Incidence," AIAA Paper 90-0096, Jan. 1990.